Detection of gaseous nerve agent simulants with broadband photoacoustic spectroscopy

Mikkonen, Tommi

2022-10-15

Mikkonen , T , Luoma , D , Hakulinen , H I , Goery Genty , G , Vanninen , P & Toivonen , J 2022 , ' Detection of gaseous nerve agent simulants with broadband photoacoustic spectroscopy ' , Journal of Hazardous Materials , vol. 440 , 129851 . https://doi.org/10.1016/j.jhazmat.2022.129851

http://hdl.handle.net/10138/351994
https://doi.org/10.1016/j.jhazmat.2022.129851

Journal of Hazardous Materials 440 (2022) 129851

Contents lists available at ScienceDirect

Journal of Hazardous Materials

journal homepage: www.elsevier.com/locate/jhazmat

Research Paper

Detection of gaseous nerve agent simulants with broadband photoacoustic spectroscopy

Tommi Mikkonen [a,*,1], Daniel Luoma [a], Hanna Hakulinen [b,2], Goëry Genty [a,3], Paula Vanninen [b,4], Juha Toivonen [a,5]

[a] Photonics Laboratory, Physics Unit, Tampere University, Tampere, Finland
[b] Finnish Institute for Verification of the Chemical Weapons Convention (VERIFIN), Department of Chemistry, University of Helsinki, Helsinki, Finland

HIGHLIGHTS

- Sub-ppm detection of nerve agent simulants.
- Low gas consumption of a few milliliters.
- High selectivity and possibility for multi-species detection.
- Fast response and recovery times.

GRAPHICAL ABSTRACT

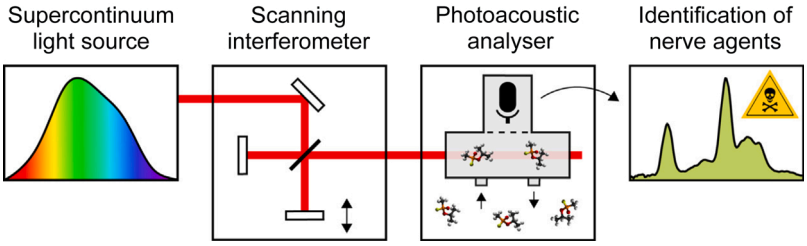

ARTICLE INFO

Keywords:
Chemical warfare agent
Fourier transform spectroscopy
Supercontinuum
Gas phase

ABSTRACT

While recent high-profile assassination attempts have once again brought nerve agents (NAs) into the spotlight, the current portfolio of NA sensors lack a sufficient combination of high performance and field-deployability. Here, we report a novel optical sensor for the detection of gaseous NAs with a potential to fill this gap. The technique is based on Fourier transform spectroscopy with a supercontinuum (SC) light source and cantilever-enhanced photoacoustic detection providing fast multi-species gas sensing with high sensitivity and selectivity in a sample volume of 7 ml, which becomes advantageous when analysing limited NA samples in the field. We study the fundamental C–H stretch bands of four known NA simulants and achieve detection limits of 64–530 ppb in one minute and recovery times of a few minutes. In the near future, the technique has significant potential to improve through the development of more powerful SC sources further in the mid-infrared region.

* Correspondence to: Faculty of Engineering and Natural Sciences,Tampere University, Finland.
E-mail address: tommi.mikkonen@tuni.fi (T. Mikkonen).
[1] 0000-0001-7511-2910
[2] 0000-0001-7049-1659
[3] 0000-0002-0768-3663
[4] 0000-0001-9579-0380
[5] 0000-0003-0900-174X

https://doi.org/10.1016/j.jhazmat.2022.129851
Received 30 May 2022; Received in revised form 22 July 2022; Accepted 24 August 2022
Available online 28 August 2022

1. Introduction

The widespread use of chemical warfare agents (CWAs) was initiated in World War I, and despite international efforts to ban their production, stockpiling and exploitation under the Chemical Weapons Convention (1997), CWAs have remained a serious threat in both military and civilian scenarios (Chauhan et al., 2008; Sanderson et al., 2009). An especially lethal class of CWAs are nerve agents (NAs) whose first extensive deployments were in the Iran–Iraq war (1980–88) (Haines and Fox, 2014) and the terrorist attacks in Japan (1994–95) (Seto et al., 2000; Okumura et al., 1996). Recently, NAs have once again ended up at the center of public attention due to incidents in the ongoing Syrian civil war (2011–) (Pita and Domingo, 2014; United Nations, 2013), the assassination of Kim Jong-Nam in Malaysia (2017) (U.S. Department of State, 2020) and the assassination attempts of Sergei Skripal in the United Kingdom (2018) (Vale et al., 2018; Organisation for the Prohibition of Chemical Weapons, 2018a) and Alexei Navalny in Russia (2020) (Organisation for the Prohibition of Chemical Weapons, 2018b).

The toxicity of NAs stem from their ability to irreversibly disrupt the communication of the nervous system, which leads to a wide range of severe consequences depending on the type and dose of the agent and the route of exposure (Costanzi et al., 2018). The most effective passage of NAs into human body is through the respiratory system, where the typically liquid agents can end up as aerosols or vapours due to the volatility of the NAs (e.g., 2800 parts per million (ppm) and 49 ppm for sarin and tabun, respectively, at 20 ˚C) (Wiener and Hoffman, 2004). Already extremely low NA doses are hazardous, lethal concentrations being 12 ppm and 22 ppm in one minute for gaseous sarin and tabun, respectively (Costanzi et al., 2018), and thus parts per billion (ppb) level detection of these substances in the gas phase is essential. Moreover, NAs are typically detected from urban air or heated liquid/solid field samples with varying concentrations of interfering species, calling for extremely high selectivity against numerous compounds.

The development of NA sensors is largely directed towards portable devices for on-site identification with a fast response time and as high sensitivity and selectivity as possible. The simplest detectors such as electrochemical (Liu and Lin, 2005), colorimetric (Davidson et al., 2020) and fluorimetric sensors (Khan et al., 2018; Meng et al., 2021), surface acoustic wave detectors (Kim et al., 2020) and ion-mobility spectrometers (Puton and Namieśnik, 2016) provide a low-cost option for screening, but they suffer from poor sensitivity, insufficient selectivity and/or susceptibility to changes in temperature and humidity. Technologies with improved performance include gas chromatography mass spectrometry (Smith et al., 2004), Raman spectroscopy (Lafuente et al., 2020) and infrared absorption spectroscopy (Pushkarsky et al., 2006; Mukherjee et al., 2008; Gurton et al., 2012; Levy, 2009; Sharpe et al., 2003; Ruiz-Pesante et al., 2007; Ohrui et al., 2020; Melkonian et al., 2020), which are preferred in different scenarios due to their specific characteristics. Infrared absorption spectroscopy is typically well suited for rapid identification of volatile NAs in ambient air, techniques ranging from extremely sensitive photoacoustic spectroscopy (PAS) (Pushkarsky et al., 2006; Mukherjee et al., 2008; Gurton et al., 2012) to Fourier transform infrared spectroscopy (FTIR) (Sharpe et al., 2003; Ruiz-Pesante et al., 2007; Ohrui et al., 2020) capable of selective multi-species detection.

These two complementary methods have long been combined in Fourier transform photoacoustic spectroscopy (FT-PAS) (Farrow et al., 1978), which utilizes the parallel down-conversion of optical frequencies of a broadband light into acoustic frequencies, followed by the excitation of absorption-induced pressure waves through periodic thermal relaxations. However, only recent advances in light sources and pressure transducers have fully realized the potential of the technique (Karhu et al., 2019; Mikkonen et al., 2018, 2022b; Sadiek et al., 2018; Wildi et al., 2020). For example, we have previously implemented a supercontinuum (SC) source and a cantilever microphone in a FT-PAS system, which provides fast and selective sensing of hydrocarbons with ppb-level detection limits in a few milliliter sample volume (Mikkonen et al., 2022b).

Here, we apply FT-PAS to the detection of gaseous NAs by analysing four known NA simulants. We utilize the volatility of the simulants in sampling, where the low gas consumption speeds up the gas exchange process, simplifies the cleaning of the gas cell and would enable the analysis of NA samples with limited availability, a realistic real-life scenario. We examine the unique C–H stretch bands of these species and report our sensor's high performance in terms of detection limits (ppb-level), selectivity and recovery time (a few minutes), convincing the applicability of FT-PAS in reliable and rapid identification of NAs.

2. Materials and methods

2.1. Experimental setup

The experimental setup illustrated in Fig. 1 closely resembles our previously reported system (Mikkonen et al., 2022b) and has a footprint of about 40 kg and 50 cm × 35 cm × 35 cm when enclosed tightly. The radiation source is a home-built SC (Mikkonen et al., 2018; Amiot et al., 2017), where sub-nanosecond pulses from an erbium-doped fiber laser (1547 nm, 6464 cm^{-1}) are injected into two successive optical fibers (a 4-m-long silica dispersion-shifted fiber and an 8.3-m-long fluoride fiber) at 90 kHz repetition rate. The outcome is extensive spectral broadening of the pump up to 3600 nm (2800 cm^{-1}) in the long wavelength side. After collimation (2 mm beam diameter), the SC light is spectrally filtered to remove optical power outside the usable wavenumber region, which eliminates water absorption around 3800 cm^{-1} and therefore significantly reduces noise (Mikkonen et al., 2022a). A unitless envelope of this filtered SC is shown in the bottom-left corner in Fig. 1 (black line), obtained from a measured (monochromator, Spectral Products DK480 1/2) and post-processed (spectral filtering) spectrum of the SC.

The filtered SC light is directed into a scanning Michelson interferometer (Bruker IRCube), where a slow optical path difference scan velocity of about 0.1 cm/s results in the down-conversion of optical frequencies 2800–3400 cm^{-1} into acoustic frequencies 280–340 Hz. This wavenumber-dependent intensity modulation of the light source is schematically illustrated in the bottom-left corner in Fig. 1. The maximum spectral resolution of the interferometer is 1 cm^{-1}, but a lower resolution of 4 cm^{-1} is selected for this work as the absorption features of NA simulants are relatively broad. For this resolution, a single scan is acquired in five seconds.

The intensity-modulated SC light with 7 mW of optical power is focused into a photoacoustic (PA) analyser (Gasera PA201) and a homebuilt multipass cell (Mikkonen et al., 2022b) which reflects the SC beam ten times through a small cylindrical gas cell (95 mm long, 4 mm in diameter, about 7 ml by total volume). The cumulative power spectral density (PSD) of the SC inside this non-resonant gas cell is shown in Fig. 2a, taking into account the transmittance of the anti-reflection coated BaF_2 windows and a constant 2% loss of the mirrors. The absorption-induced sound waves are detected using an optically read silicon cantilever with a thickness of a few μm, an area of a few mm^2 and a characteristic resonance frequency at 700 Hz (note that the cantilever is operated off-resonance) (Koskinen et al., 2008). The displacement of the cantilever is monitored with a spatial-type interferometer (Kuusela and Kauppinen, 2007). The interferogram recorded by the cantilever microphone is windowed (a three-term Blackman-Harris (Naylor and Tahic, 2007)) and Fourier transformed to obtain a background-free absorption spectrum of the gas species inside the cell.

2.2. Materials and sampling

We analyse four NA simulants, namely trimethyl phosphate (TMP, Sigma-Aldrich, >99%), dimethyl methylphosphonate (DMMP, Fluka, 97%), diethyl methylphosphonate (DEMP, Sigma-Aldrich, 97.3%) and diisopropyl methylphosphonate (DIMP, Alfa Aesar, 95%), whose

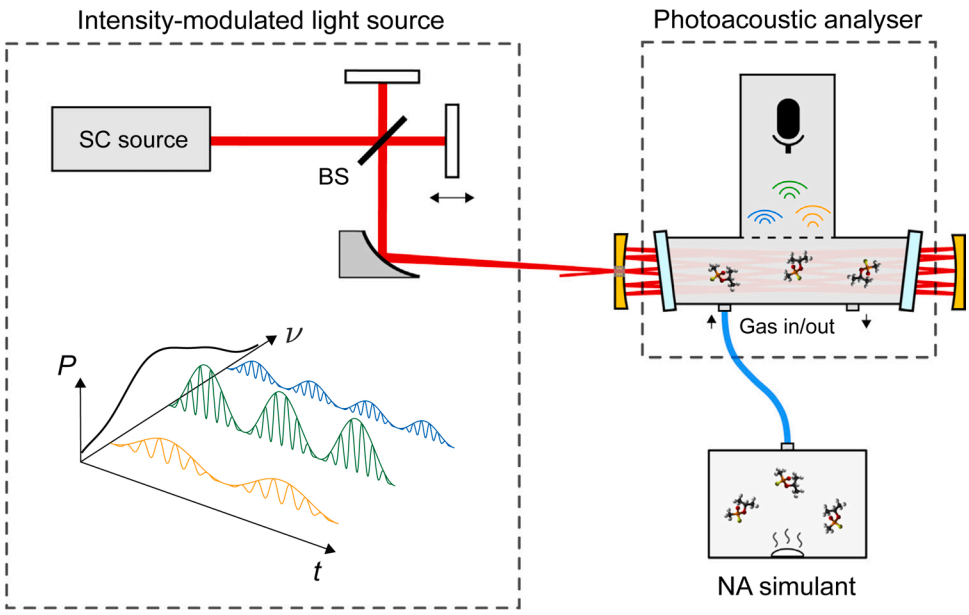

Fig. 1. A schematic of the experimental setup: SC - supercontinuum; BS - beamsplitter; P - optical power; ν - wavenumber; t - time; NA - nerve agent. Wavenumber-dependent intensity modulation of the SC source is illustrated in the bottom left corner, where the relative frequencies are exaggerated. The absolute wavenumber scale of the SC spectrum is shown in Fig. 2a.

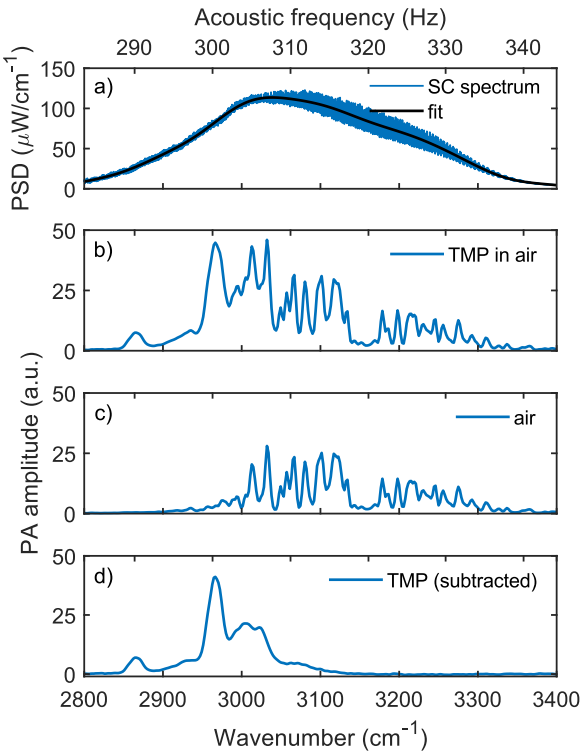

Fig. 2. a) Effective power spectral density (PSD) spectrum of the SC radiation inside the gas cell, measured FT-PAS spectrum of b) TMP in air and c) pure air (4 cm^{-1} resolution, 60 s measurement time), and d) post-processed spectrum of TMP.

molecular structures and thus spectral properties are similar to G-series NAs such as sarin, tabun and soman (Ruiz-Pesante et al., 2007; Mott and Rez, 2012; Neupane et al., 2019; Kumar et al., 2019). Simulant samples in the gas phase are prepared by placing 20 μl of liquid simulant at the bottom of a one-liter container as illustrated at the bottom-right corner in Fig. 1. The liquid simulant in the sampling container is rested for at least one hour to evaporate, after which the equilibrium vapour pressure at room temperature is assumed to be reached. From the headspace of the container, the gas phase simulants mixed in laboratory air are pumped into the gas cell using a gas exchange system incorporated into the PA analyser. Considering the time to exchange the gas and the time to record a single spectrum, the response time of the sensor is less than ten seconds.

2. Results and discussion

2.1. Data processing

The measured raw absorption spectrum of TMP in air averaged over 12 scans (one minute) is shown in Fig. 2b. Interfering absorption features in the high-frequency side of the spectrum are from water vapour which dominates the absorption spectrum of air in this spectral region. This interference is eliminated by recording a spectrum of laboratory air (Fig. 2c), fitting that to the TMP-free region (3200–3400 cm^{-1}) of the raw spectrum to account for small changes in the water concentration, and subtracting the fitted water spectrum from the raw spectrum. The linear least squares spectral fitting algorithm was implemented using Matlab's linsolve function which solves the matrix equation $Ax = B$ using QR factorization with column pivoting. The same algorithm was employed in all spectral fitting procedures appearing later in this work. The resulting spectrum of pure TMP is shown in Fig. 2d, which is then corrected by the spectral envelope of the SC inside the gas cell shown in black in Fig. 2a.

Corrected FT-PAS spectra of TMP and other simulants are shown in Fig. 3 together with absorption cross section spectra recorded with a conventional FTIR system (Neupane et al., 2019). The measurements agree with each other, FT-PAS spectra exhibiting higher signal-to-noise ratios (SNRs). We note that a small TMP residual was subtracted from the DEMP spectrum. Different magnitudes in the measured spectra result from differences in the absorption cross sections and the concentrations of the simulants inside the cell. These concentrations, which depend on the equilibrium vapour pressures and adsorption properties of the simulant molecules, can be estimated after calibrating the system.

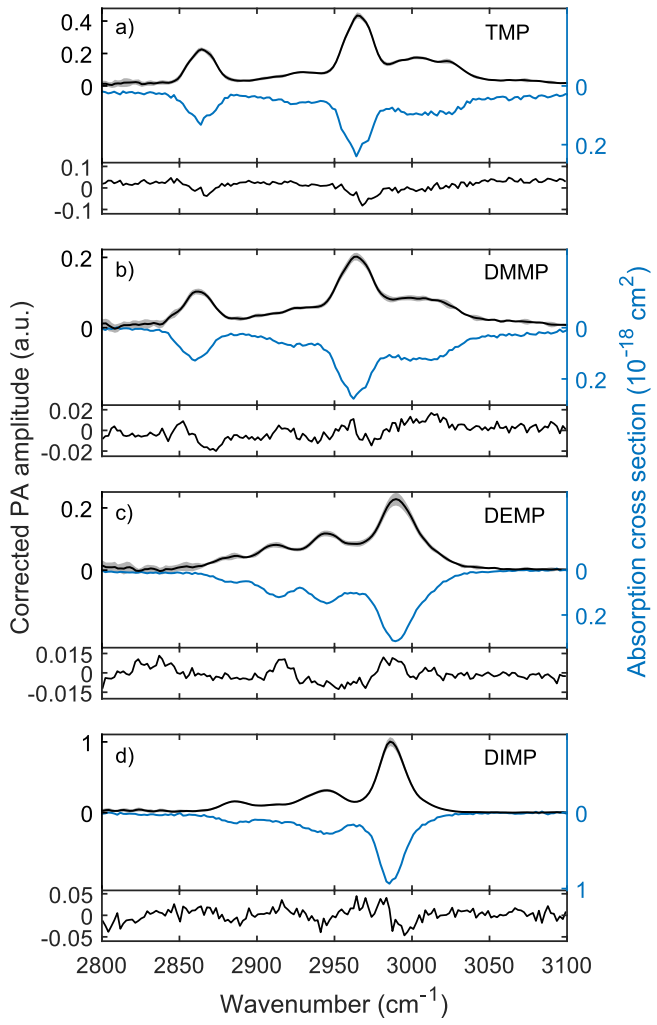

Fig. 3. Measured, water-subtracted and PSD-corrected FT-PAS spectra (left axis) and FTIR reference (Neupane et al., 2019) (right axis, inverted) of a) TMP, b) DMMP, c) DEMP and d) DIMP. The average of 12 scans is shown in black and the standard deviation in grey for the FT-PAS spectra. Lower panels show the residuals between these two approaches, acquired by scaling the reference absorption cross sections.

2.2. Calibration

Calibration is required in PAS to relate the recorded PA amplitude with the target gas concentration. The calibration process utilizes linear dependence of the wavenumber ν dependent PA amplitude $S(\nu)$ on optical power $P(\nu)$, absorption cross section $\sigma(\nu)$ and concentration c,

$$S(\nu) = \Lambda(\nu) * [AP(\nu)\sigma(\nu)c] = AP(\nu)\widehat{\sigma}(\nu)c, \quad (1)$$

where $\Lambda(\nu)$ is the instrument lineshape function (Fourier transform of the window function), A is the calibration constant, the symbol * denotes convolution and $\widehat{\sigma}(\nu) = \Lambda(\nu) * \sigma(\nu)$. The instrument lineshape function does not affect the smoothly varying SC spectral envelope.

As we currently have no reliable way to estimate nor vary the gas phase simulant concentrations in the gas cell, we characterized the calibration constant A by recording the absorption spectrum (fundamental asymmetric C–H stretch band) of methane (CH_4) with controlled volume mixing ratios between 0.2 and 50 ppm. These volume concentrations were prepared by mixing CH_4 from a 400 ppm gas bottle with nitrogen using two mass flow controllers (Bronkhorst F-201CV). For simplicity, we only analyzed a single wavenumber (ν_{max}) corresponding to the strongest PA amplitude of CH_4 and measured the linear proportionality constant between $S(\nu_{max})$ and c. We divided this constant by $P(\nu_{max})$ and $\widehat{\sigma}(\nu_{max})$, which was calculated by convolving the absorption cross section spectrum of CH_4 (from the HITRAN database (Rothman et al., 2013)) with the instrument lineshape function. This division yields the calibration constant A for CH_4.

Univocal calibration constant for different gas species necessitates constant non-radiative relaxation efficiency (here incorporated into A) between the considered species and possible gas mediums, which in general is not the case in PAS (Russo et al., 2021; Müller et al., 2022). However, the situation is considerably simplified here as our modulation frequencies around 300 Hz are unconventionally low for PAS and most importantly lower than the molecular relaxation rates in our gas matrices (Müller et al., 2022; Barreiro et al., 2012). Complete thermal relaxation enables the transfer of the calibration constant of CH_4 to simulant substances and nerve agents. Simulant concentrations can then be calculated from Eq. 1, where the absorption cross sections of the simulants are collected from the reference FTIR data in Fig. 3. Again, only single wavenumbers corresponding to the maximum absorption cross sections of the simulants are utilized.

Using this calibration procedure, we estimated the simulant concentrations to be in the range of 110–300 ppm in the gas cell as summarized in the second column in Table 1. These concentrations are on average 35% from the initial concentrations in the sampling container (estimated from the vapour pressures of the simulants at 20 °C (Butrow et al., 2009; Cuisset et al., 2008)) due to the adsorption of simulant molecules on the sampling equipment and the surfaces of the gas cell. Sampling efficiencies (η_s), i.e., the relations between the concentrations in the gas cell and the sampling container, are listed in the third column in Table 1. The observed variations result from measurement errors and various parameters affecting the adsorption process such as polarity and molecular weight (Li et al., 2020). Lower sampling efficiencies of about 10% have been reported for a conventional FTIR system (Ohrui et al., 2020), most likely caused by the significantly larger volume of the gas equipment. The uncertainties in the calibrated simulant concentrations shown in the rightmost column of Table 1 include errors in the calibration constant A (0.5% from the fitting, 3.1% from optical power (Mikkonen et al., 2022b), and 5% from the absorption cross section of CH_4 (Daumont et al., 2013)), absorption cross sections of simulants (6.2–12% (Neupane et al., 2019)) and optical power again (3.1% (Mikkonen et al., 2022b)).

2.3. Detection limits

We estimated the limits of detection (LODs) for all simulants using LOD = $3Nc/S$, where S is the strongest PA amplitude of the simulant in the water-corrected spectrum and N is the noise level, calculated as the standard deviation of a non-absorbing part (2000–2800 cm^{-1}) of the water spectrum. The noise level is calculated from a measurement involving no simulant molecules in the gas cell, because significant simulant absorption raises the noise level (Mikkonen et al., 2022a). Calculated detection limits for one minute averaging and corresponding to the minimum concentrations that can be detected inside the gas cell are shown in the fourth column in Table 1. To illustrate the validity of

Table 1
Estimated concentrations of four simulants in the gas cell, sampling efficiencies η_s, calculated limits of detection (LODs) in 60 s for simulant samples inside or outside the gas cell, and relative uncertainties in the concentrations and LODs.

Simulant	c (ppm)	η_s (%)	LOD (ppb)		Δc (%)
			In	Out	
TMP	310	36	130	360	14
DMMP	160	20	110	530	10
DEMP	160	43	79	190	10
DIMP	120	42	26	64	10

this unconventional determination of the detection limit, we measured a small concentration (230 ppb) of DIMP in which case the noise induced by the simulant is negligible and the LOD can be obtained directly from the SNR of the spectrum. A single water-subtracted scan of this measurement is shown in Fig. 4 with a SNR of 7.7 ± 0.3 corresponding to a LOD of 26 ± 1 ppb in 60 s, in perfect agreement with the value in Table 1. The uncertainty includes only the fitting error (no calibration error).

In order to estimate the detection limits that can be reached from samples outside the sensor, the LOD values in the fourth column in Table 1 were divided by the corresponding sampling efficiencies resulting in values of 64–530 ppb (the fifth column in Table 1). By comparing the absorption cross sections of sarin and TMP (Sharpe et al., 2003; Neupane et al., 2019) and assuming 35% sampling efficiency, we estimated a detection limit of 180 ± 40 ppb for sarin which is approximately an order of magnitude higher compared to a LOD achieved with a commercial, high-performance and field-portable FTIR system when normalized by the acquisition time (Ohrui et al., 2020). However, it should be noted that the required sample volume of our system is 57 times smaller and the FTIR system capitalizes on stronger P–O–C stretch bands around 1000 cm^{-1}.

2.4. Selectivity

Similar features in the C–H stretch bands of some simulants (Fig. 3) and NAs (Sharpe et al., 2003) could indicate complications in the correct identification of these species. We investigated the selectivity of our sensor by compiling a spectral library of the simulants (and water) and performing new single-component and single-scan measurements with these four substances and concentrations ranging 20–40 ppm. Using the spectral library and the least squares spectral fitting algorithm, we estimated the concentration of each species in the gas cell. For each simulant, we repeated this process for five scans, averaged the retrieved concentrations simulant-wise and calculated the absolute values (for illustration purposes as negative values cannot be displayed in a logarithmic scale). The results are shown in Fig. 5 where each row represents the outcome for a specific simulant applied in the gas cell (applied simulant on the left panel, retrieved simulants on the bottom panel).

Noting the logarithmic color scale, Fig. 5 displays good selectivity of the system. All simulants were confidently identified and the average concentration for absent species is 300 ppb (values outside the diagonal). Most remarkably, small differentiating features in the absorption spectra of TMP and DMMP are successfully recognized with no particular cross-sensitivity between these simulants. The most prominent incorrect detection was 1 ppm of DMMP in the DIMP measurement (fourth row, second column), which however may be attributed to

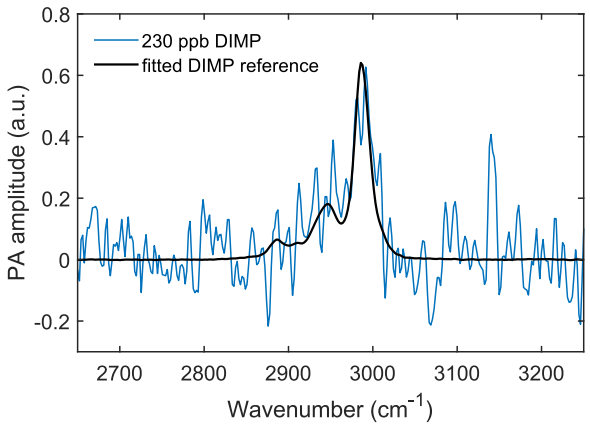

Fig. 4. A single scan, water-subtracted spectrum of 230 ppb of DIMP (blue line) and a fitted DIMP reference (black line) obtained experimentally at a high concentration.

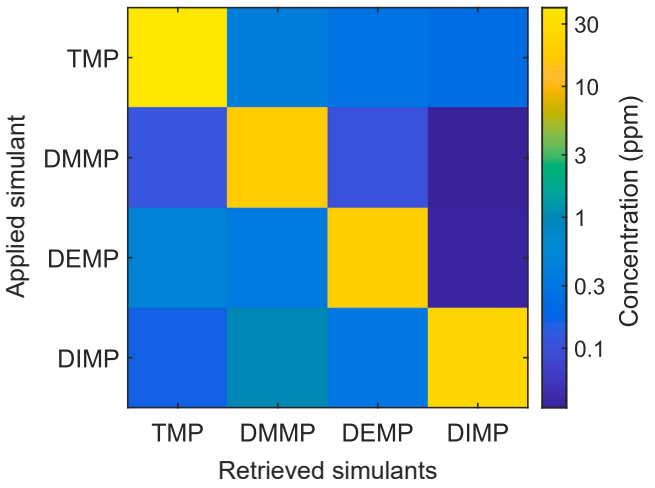

Fig. 5. An illustration of the system's selectivity, compiled from single-component and single-scan measurements of four simulants (left). For each raw spectrum, a library of simulant references was fitted to retrieve the concentrations of the simulants (bottom) in the gas cell. For each simulant, five single scans were acquired, and the final result (each row) shows absolute values of the average retrieved concentrations. Absolute values were calculated due to the logarithmic scale. For example, the analysis of the DIMP measurement is shown at the bottom row, which displays retrieved concentrations of 0.2 ppm, 1 ppm, 0.3 ppm and 30 ppm for TMP, DMMP, DEMP and DIMP, respectively. Average uncertainty in the retrieved concentrations was 42% (fitting error).

residual DMMP in the sampling container (DIMP sample was placed in a container that previously contained DMMP). Similar reasoning also holds for the second most prominent incorrect detection, 500 ppb of TMP in the DEMP measurement. This underlines the difficulty in handling volatile substances and the importance of thorough cleaning of all contaminated surfaces. Without these two doubtful incorrect identifications, the average concentration for absent species is 200 ppb, which is 0.8% from the average applied concentration and around the noise level of the high concentration (and therefore high noise level) measurements.

2.5. Recovery time

An important feature for a NA sensor is the ability to recover fast after encountering high concentrations. In our system, recovery time is limited by the gas adsorption onto the inner surface of the gas cell and the pump system whereof it evaporates back into gas phase after the cell is purged with clean air. It is therefore favourable to change the gas sample inside the cell after each scan which was the procedure in all our measurements. The duration of this cleaning depends on the substance, its initial concentration in the gas cell and the concentration in which the substance cannot be anymore detected, high initial concentrations of sticky molecules with low detection limits exhibiting the longest recovery times. Therefore, we characterized the cleaning of the gas equipment in the worst scenario by injecting a high concentration (100 ppm) of DIMP in the gas cell. We repeated 71 times a sequence of flushing the cell with clean air for two seconds and recording a single spectrum. The concentration of DIMP was retrieved from each raw spectrum by fitting DIMP and water references to the spectrum, and the result of this investigation is shown in Fig. 6.

The concentration of DIMP decreases three orders of magnitude during the flushing procedure. A three-term exponential function was fitted to the concentration trace as three separate evaporation processes are present in the system: one in the gas cell and two in the two gas tube systems delivering the sample in the cell. These three contributions are shown in Fig. 6. The sampling tubes are efficiently cleaned within the

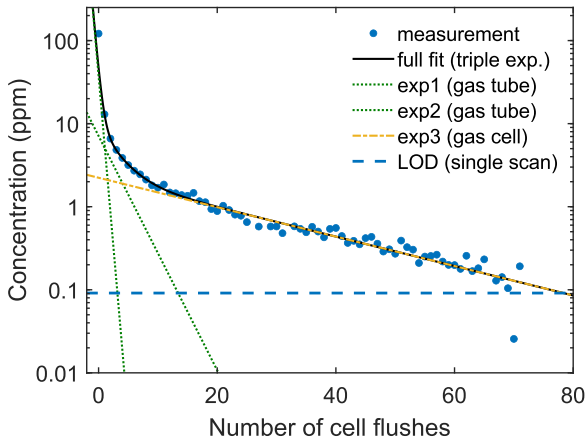

Fig. 6. Concentration of DIMP (blue dots) for increasing number of 2 s flushes of the gas cell with clean air, triple exponential fit (solid black line), three components of the fit (dashed green and yellow lines) and the limit of detection in 5 s (dashed blue line).

first ten flushes, after which the DIMP concentration decreases more slowly and is dominated by the adsorbed substance in the gas cell. From the fitted line, we can estimate the number of flushes required to decrease the simulant concentration below the single-scan LOD (dashed line in Fig. 6). For DIMP with an initial concentration of about 100 ppm, 80 flushes correspond to a recovery time of 160 s in terms of active pumping, or ~ 12 min in terms of continuous monitoring in which a spectrum is recorded after each 2 s flush. For lower initial concentrations of DIMP and for other simulants, this time is expected to be shorter. Moreover, heated gas equipment would accelerate the recovery significantly.

4. Conclusions

We have demonstrated Fourier transform photoacoustic spectroscopy (FT-PAS) with a supercontinuum (SC) light source for the detection of gaseous nerve agents (NAs). This approach combines the broadband nature of Fourier transform spectroscopy with the high sensitivity of cantilever-enhanced PAS for a field-deployable sensor with high performance. We analysed the C–H stretch bands of four NA simulants whose measured absorption spectra were in a good agreement with the literature (Neupane et al., 2019). We achieved detection limits of 64–530 ppb in 60 s for the simulants, which should be considered in the context of the system's low gas consumption (7 ml), high selectivity and the possibility for simultaneous multi-species detection (Mikkonen et al., 2022b). While our attained detection sensitivity is an order of magnitude worse compared to a conventional FTIR system with similar footprint (Ohrui et al., 2020), the required sample volume is nearly 60 times smaller providing a significant advantage when analysing field samples with limited availability. Furthermore, low gas consumption increases the sampling efficiency and is expected to decrease the recovery time of the sensor, which for our system was demonstrated to be in the range of a few minutes for an initially high sample concentration.

The performance of the sensor could be significantly enhanced by analysing the stronger and more selective P–O–C stretch bands further in the mid-infrared region (Sharpe et al., 2003; Neupane et al., 2019), where commercial SC sources are currently not available but expected in the near future. This would be especially beneficial when dealing with complex samples that require the construction of a spectral library containing all expected interferents. However, the current sensor operating around 3000 cm^{-1} has been demonstrated to perform sufficiently in multi-species hydrocarbon detection (Mikkonen et al., 2022b). In this spectral region, the sensitivity can most simply be enhanced by using a SC source with higher power spectral density and optimizing the multipass cell with better windows. In addition to temporal averaging (Mikkonen et al., 2022b), the detection limits could be further lowered by a factor of six with higher sampling efficiency (by heating the gas equipment), faster scanning velocity and better elimination of water absorption. The precision of the sensor is largely limited by the power variations of the light source, which can be eliminated by continuous power monitoring. Furthermore, the accuracy could be improved with a better calibration against a reference sensor. Especially with these advancements, the demonstrated technique provides a novel and complementary tool for high-performance identification of NAs for example in the diagnosis of poisoning and forensic investigation.

Environmental implication

The materials studied in this work are four organophosphorus compounds, which themselves possess a moderate health hazard. However, here we use these compounds to simulate volatile nerve agents such as sarin, soman and tabun, which are one of the most lethal chemical weapons. Our work presents a novel technique for the detection of gaseous nerve agents with high performance and low sample consumption. The approach provides a complementary tool for the analysis of complex field samples with limited availability, thus contributing to faster and more reliable identification for forensic investigation, the diagnosis and treatment of poisoning and occupational health monitoring.

CRediT authorship contribution statement

Tommi Mikkonen: Conceptualization, Methodology, Formal analysis, Investigation, Writing – original draft, Visualization. **Daniel Luoma:** Investigation, Data curation. **Hanna Hakulinen:** Conceptualization, Resources. **Goëry Genty:** Resources, Writing – review & editing. **Paula Vanninen:** Conceptualization, Resources. **Juha Toivonen:** Conceptualization, Resources, Writing – review & editing, Supervision.

Declaration of Competing Interest

The authors declare that they have no known competing financial interests or personal relationships that could have appeared to influence the work reported in this paper.

Data Availability

Data will be made available on request.

Acknowledgements

This work was supported by the Graduate School of Tampere University and the Academy of Finland Flagship Programme PREIN (grant 320165).

References

Amiot, C., Aalto, A., Ryczkowski, P., Toivonen, J., Genty, G., 2017. Cavity enhanced absorption spectroscopy in the mid-infrared using a supercontinuum source. Appl. Phys. Lett. 111 (6), 061103.
Barreiro, N., Peuriot, A., Santiago, G., Slezak, V., 2012. Water-based enhancement of the resonant photoacoustic signal from methane–air samples excited at 3.3 μm. Appl. Phys. B 108 (2), 369–375.
Butrow, A.B., Buchanan, J.H., Tevault, D.E., 2009. Vapor pressure of organophosphorus nerve agent simulant compounds. J. Chem. Eng. Data 54 (6), 1876–1883.
Chauhan, S., R.D′cruz, Faruqi, S., Singh, K., Varma, S., Singh, M., Karthik, V., 2008. Chemical warfare agents. Environ. Toxicol. Pharmacol. 26 (2), 113–122.
Costanzi, S., Machado, J.-H., Mitchell, M., 2018. Nerve agents: what they are, how they work, how to counter them. ACS Chem. Neurosci. 9 (5), 873–885.
Cuisset, A., Mouret, G., Pirali, O., Roy, P., Cazier, F., Nouali, H., Demaison, J., 2008. Gas-phase vibrational spectroscopy and ab initio study of organophosphorous compounds: Discrimination between species and conformers. J. Phys. Chem. B 112 (39), 12516–12525.

Daumont, L., Nikitin, A., Thomas, X., Régalia, L., VonderHeyden, P., Tyuterev, V.G., Rey, M., Boudon, V., Wenger, C., Loëte, M., et al., 2013. New assignments in the 2 μm transparency window of the $^{12}CH_4$ Octad band system. J. Quant. Spectrosc. Radiat. Transf. 116, 101–109.

Davidson, C.E., Dixon, M.M., Williams, B.R., Kilper, G.K., Lim, S.H., Martino, R.A., Rhodes, P., Hulet, M.S., Miles, R.W., Samuels, A.C., et al., 2020. Detection of chemical warfare agents by colorimetric sensor arrays. ACS Sens. 5 (4), 1102–1109.

Farrow, M.M., Burnham, R.K., Eyring, E.M., 1978. Fourier-transform photoacoustic spectroscopy. Appl. Phys. Lett. 33 (8), 735–737.

Gurton, K.P., Felton, M., Tober, R., 2012. Selective real-time detection of gaseous nerve agent simulants using multiwavelength photoacoustics. Opt. Lett. 37 (16), 3474–3476.

Haines, D.D., Fox, S.C., 2014. Acute and long-term impact of chemical weapons: lessons from the Iran-Iraq war. Forensic Sci. Rev. 26 (2), 97–114.

Karhu, J., Tomberg, T., Vieira, F.S., Genoud, G., Hänninen, V., Vainio, M., Metsälä, M., Hieta, T., Bell, S., Halonen, L., 2019. Broadband photoacoustic spectroscopy of $^{14}CH_4$ with a high-power mid-infrared optical frequency comb. Opt. Lett. 44 (5), 1142–1145.

Khan, M.S.J., Wang, Y.-W., Senge, M.O., Peng, Y., 2018. Sensitive fluorescence on-off probes for the fast detection of a chemical warfare agent mimic. J. Hazard. Mater. 342, 10–19.

Kim, J., Kim, E., Kim, J., Kim, J.-H., Ha, S., Song, C., Jang, W.J., Yun, J., 2020. Four-channel monitoring system with surface acoustic wave sensors for detection of chemical warfare agents. J. Nanosci. Nanotechnol. 20 (11), 7151–7157.

Koskinen, V., Fonsen, J., Roth, K., Kauppinen, J., 2008. Progress in cantilever enhanced photoacoustic spectroscopy. Vib. Spectrosc. 48 (1), 16–21.

Kumar, N., Tiwari, K.R., Meenu, K., Sharma, A., Jain, A., Singh, S., Tomar, R., et al., 2019. Utilization of various analogy of synthetic nanoporous zeolites and composite of zeolites for decontamination/detoxification of CWA simulants—an updated review. Int. J. Nonferrous Metall. 8 (04), 35.

Kuusela, T., Kauppinen, J., 2007. Photoacoustic gas analysis using interferometric cantilever microphone. Appl. Spectrosc. Rev. 42 (5), 443–474.

Lafuente, M., Sanz, D., Urbiztondo, M., Santamaría, J., Pina, M.P., Mallada, R., 2020. Gas phase detection of chemical warfare agents CWAs with portable Raman. J. Hazard. Mater. 384, 121279.

Levy, D., 2009. Advances in portable FTIR spectrometers for the field: the HazMatID Ranger. In: Next-Generation Spectroscopic Technologies II, Vol. 7319. International Society for Optics and Photonics, p. 73190E (p).

Li, X., Zhang, L., Yang, Z., Wang, P., Yan, Y., Ran, J., 2020. Adsorption materials for volatile organic compounds (VOCs) and the key factors for VOCs adsorption process: a review. Sep. Purif. Technol. 235, 116213.

Liu, G., Lin, Y., 2005. Electrochemical sensor for organophosphate pesticides and nerve agents using zirconia nanoparticles as selective sorbents. Anal. Chem. 77 (18), 5894–5901.

Melkonian, J.-M., Armougom, J., Raybaut, M., Dherbecourt, J.-B., Gorju, G., Cézard, N., Godard, A., Pašiškevičius, V., Coetzee, R., Kadlčák, J., 2020. Long-wave infrared multi-wavelength optical source for standoff detection of chemical warfare agents. Appl. Opt. 59 (35), 11156–11166.

Meng, W., Pei, Z., Wang, Y., Sun, M., Xu, Q., Cen, J., Guo, K., Xiao, K., Li, Z., 2021. Two birds with one stone: The detection of nerve agents and AChE activity with an ICT-ESIPT-based fluorescence sensor. J. Hazard. Mater. 410, 124811.

Mikkonen, T., Eslami, Z., Genty, G., Toivonen, J., 2022a. Supercontinuum intensity noise coupling in Fourier transform photoacoustic spectroscopy. Opt. Lett. 47 (7), 1713–1716.

Mikkonen, T., Hieta, T., Genty, G., Toivonen, J., 2022b. Sensitive multi-species photoacoustic gas detection based on mid-infrared supercontinuum source and miniature multipass cell. Phys. Chem. Chem. Phys. 24, 19481–19487.

Mikkonen, T., Amiot, C., Aalto, A., Patokoski, K., Genty, G., Toivonen, J., 2018. Broadband cantilever-enhanced photoacoustic spectroscopy in the mid-IR using a supercontinuum. Opt. Lett. 43 (20), 5094–5097.

Mott, A.J., Rez, P., 2012. Calculated infrared spectra of nerve agents and simulants. Spectrochim. Acta Part A: Mol. Biomol. Spectrosc. 91, 256–260.

Mukherjee, A., Dunayevskiy, I., Prasanna, M., Go, R., Tsekoun, A., Wang, X., Fan, J., Patel, C.K.N., 2008. Sub-parts-per-billion level detection of dimethyl methyl phosphonate (DMMP) by quantum cascade laser photoacoustic spectroscopy. Appl. Opt. 47 (10), 1543–1548.

Müller, M., Rück, T., Jobst, S., Pangerl, J., Weigl, S., Bierl, R., Matysik, F.-M., 2022. An algorithmic approach to compute the effect of non-radiative relaxation processes in photoacoustic spectroscopy. Photoacoustics, 100371.

Naylor, D.A., Tahic, M.K., 2007. Apodizing functions for Fourier transform spectroscopy. JOSA A 24 (11), 3644–3648.

Neupane, S., Peale, R., Vasu, S., 2019. Infrared absorption cross sections of several organo-phosphorous chemical-weapon simulants. J. Mol. Spectrosc. 355, 59–65.

Ohrui, Y., Hashimoto, R., Ohmori, T., Seto, Y., Inoue, H., Nakagaki, H., Yoshikawa, K., McDermott, L., 2020. Continuous monitoring of chemical warfare agents in vapor using a Fourier transform infra-red spectroscopy instrument with multi pass gas cell, mercury cadmium telluride detector and rolling background algorithm. Forensic Chem. 21, 100292.

Okumura, T., Takasu, N., Ishimatsu, S., Miyanoki, S., Mitsuhashi, A., Kumada, K., Tanaka, K., Hinohara, S., 1996. Report on 640 victims of the Tokyo subway sarin attack. Ann. Emerg. Med. 28 (2), 129–135.

Organisation for the Prohibition of Chemical Weapons, 2018a. Summary of the report on activities carried out in support of a request for technical assistance by the United Kingdom of Great Britain and Northern Ireland, (Accessed 23 September 2021) https://www.opcw.org/sites/default/files/documents/S_series/2018/en/s-1612–2018_e1.pdf.

Organisation for the Prohibition of Chemical Weapons, 2018b. Summary of the report on activities carried out in support of a request for technical assistance by Germany, (Accessed 23 September 2021) https://www.opcw.org/documents/2020/10/s19062020/note-technical-secretariat-summary-report-activities-carried-out.

Pita, R., Domingo, J., 2014. The use of chemical weapons in the Syrian conflict. Toxics 2 (3), 391–402.

Pushkarsky, M.B., Webber, M.E., Macdonald, T., Patel, C.K.N., 2006. High-sensitivity, high-selectivity detection of chemical warfare agents. Appl. Phys. Lett. 88 (4), 044103.

Puton, J., Namieśnik, J., 2016. Ion mobility spectrometry: current status and application for chemical warfare agents detection. TrAC Trends Anal. Chem. 85, 10–20.

Rothman, L., Gordon, I., Babikov, Y., Barbe, A., Benner, D.C., Bernath, P., Birk, M., Bizzocchi, L., Boudon, V., Brown, L., Campargue, A., Chance, K., Cohen, E., Coudert, L., Devi, V., Drouin, B., Fayt, A., Flaud, J.-M., Gamache, R., Harrison, J., Hartmann, J.-M., Hill, C., Hodges, J., Jacquemart, D., Jolly, A., Lamouroux, J., Roy, R.L., Li, G., Long, D., Lyulin, O., Mackie, C., Massie, S., Mikhailenko, S., Müller, H., Naumenko, O., Nikitin, A., Orphal, J., Perevalov, V., Perrin, A., Polovtseva, E., Richard, C., Smith, M., Starikova, E., Sung, K., Tashkun, S., Tennyson, J., Toon, G., Tyuterev, V., Wagner, G., 2013. The HITRAN2012 molecular spectroscopic database. J. Quant. Spectrosc. Radiat. Transf. 130, 4–50. HITRAN2012 special issue.

Ruiz-Pesante, O., Pacheco-Londoño, L.C., Primera-Pedrozo, O.M., Ortiz, W., Soto-Feliciano, Y.M., Nieves, D.E., Ramirez, M.L., Hernández-Rivera, S.P., 2007. Detection of simulants and degradation products of chemical warfare agents by vibrational spectroscopy. In: Chemical and Biological Sensing VIII, Vol. 6554. International Society for Optics and Photonics, p. 65540B (p).

Russo, S.D., Sampaolo, A., Patimisco, P., Menduni, G., Giglio, M., Hoelzl, C., Passaro, V. M., Wu, H., Dong, L., Spagnolo, V., 2021. Quartz-enhanced photoacoustic spectroscopy exploiting low-frequency tuning forks as a tool to measure the vibrational relaxation rate in gas species. Photoacoustics 21, 100227.

Sadiek, I., Mikkonen, T., Vainio, M., Toivonen, J., Foltynowicz, A., 2018. Optical frequency comb photoacoustic spectroscopy. Phys. Chem. Chem. Phys. 20 (44), 27849–27855.

Sanderson, H., Fauser, P., Thomsen, M., Sørensen, P.B., 2009. Human health risk screening due to consumption of fish contaminated with chemical warfare agents in the Baltic Sea. J. Hazard. Mater. 162 (1), 416–422.

Seto, Y., Tsunoda, N., Kataoka, M., Tsuge, K., Nagano, T., 2000. Toxicological analysis of victims' blood and crime scene evidence samples in the sarin gas attack caused by the Aum Shinrikyo cult. ACS Publications, pp. 318–332. Ch. 21, pp.

Sharpe, S.W., Johnson, T.J., Chu, P.M., Kleimeyer, J., Rowland, B., 2003. Quantitative infrared spectra of vapor phase chemical agents. In: Chemical and Biological Sensing IV, Vol. 5085. International Society for Optics and Photonics, pp. 19–27 (pp).

Smith, P.A., Koch, D., Hook, G.L., Erickson, R.P., Lepage, C.R.J., Wyatt, H.D., Betsinger, G., Eckenrode, B.A., 2004. Detection of gas-phase chemical warfare agents using field-portable gas chromatography–mass spectrometry systems: instrument and sampling strategy considerations. TrAC Trends Anal. Chem. 23 (4), 296–306.

U.S. Department of State, 2020. Imposition of chemical and biological weapons control and warfare elimination act sanctions on North Korea, (Accessed 23 September 2021) https://2017–2021.state.gov/imposition-of-chemical-and-biological-weapons-control-and-warfare-elimination-act-sanctions-on-north-korea/index.html.

United Nations, 2013. Report of the United Nations Mission to Investigate Allegations of the Use of Chemical Weapons in the Syrian Arab Republic on the alleged use of chemical weapons in the Ghouta area of Damascus on 21 August 2013, (Accessed 22 September 2021) https://www.un.org/zh/focus/northafrica/cwinvestigation.pdf.

Vale, J.A., Marrs, T.C., Maynard, R.L., 2018. Novichok: a murderous nerve agent attack in the UK. Clin. Toxicol. 56 (11), 1093–1097.

Wiener, S.W., Hoffman, R.S., 2004. Nerve agents: a comprehensive review. J. Intensive Care Med. 19 (1), 22–37.

Wildi, T., Voumard, T., Brasch, V., Yilmaz, G., Herr, T., 2020. Photo-acoustic dual-frequency comb spectroscopy. Nat. Commun. 11 (1), 1–6.